JGR Solid Earth

RESEARCH ARTICLE
10.1029/2021JB023033

Moho Complexity in Southern California Revealed by Local PmP and Teleseismic Ps Waves

Tianjue Li[1,2], Jiayuan Yao[1,2], Shucheng Wu[1,2], Mijian Xu[1,2], and Ping Tong[1,2,3]

[1]Division of Mathematical Sciences, School of Physical and Mathematical Sciences, Nanyang Technological University, Singapore, Singapore, [2]Earth Observatory of Singapore, Nanyang Technological University, Singapore, Singapore, [3]Asian School of the Environment, Nanyang Technological University, Singapore, Singapore

Key Points:

- A semiautomatic workflow is developed to identify and pick local PmP waves
- We construct a new Moho geometry model for southern California using local PmP and teleseismic Ps waves
- The new Moho model shows a thick crust beneath the northern end of the central and western Transverse Ranges

Supporting Information:

Supporting Information may be found in the online version of this article.

Correspondence to:

P. Tong,
tongping@ntu.edu.sg

Citation:

Li, T., Yao, J., Wu, S., Xu, M., & Tong, P. (2022). Moho complexity in southern California revealed by local PmP and teleseismic Ps waves. *Journal of Geophysical Research: Solid Earth*, *127*, e2021JB023033. https://doi.org/10.1029/2021JB023033

Received 14 AUG 2021
Accepted 3 FEB 2022

Abstract The Moho discontinuity plays an important role in crustal growth and evolution. In this study, we delineate the Moho geometry in southern California by jointly using local Moho-reflected waves PmP and teleseismic Moho-converted waves Ps. To well constrain the Moho geometry, we have developed a two-stage process to pick PmP waves and have created a reliable PmP travel time data set with a total of 10,192 picks. We have also extracted 38,648 high-quality P-wave receiver functions (RFs). The Moho depth is initially estimated via the common conversion point (CCP) stacking of RFs and then refined by inverting the PmP travel time data in a community velocity model (CVM-H, version 15.1.1). The newly built Moho geometry is generally consistent with the California Moho Model version 1.0 (CMM-1.0), that is, a shallow Moho beneath the Salton Trough (23 km), a uniformly shallow Moho beneath the Mojave Desert and the Basin and Range (<29 km), and a sliver of deep Moho under the western Peninsular Ranges, the eastern Transverse Ranges, and the western Sierra Nevada (>34 km). However, our Moho model reveals some new features different from the CMM–1.0, such as a deep Moho (~34 km) beneath the northern end of the central and western Transverse Ranges, consistent with the observation of deep seismicities due to a thick brittle crust there. We also find a gradual transition from the lower crust to the uppermost mantle beneath the western Peninsular Ranges, leading to the rareness of pickable PmP waves as well as weak Moho-converted signals there.

Plain Language Summary The Moho discontinuity situating at the bottom of Earth's crust characterizes a surface where seismic waves change velocity and chemical composition varies. PmP waves originating from crustal earthquakes are reflected waves from the outer side of Moho, and they contain important information on the geometry, velocity change, and compositional change of or across the Moho. In this study, we have developed a semiautomatic workflow to identify the Moho-reflected signals PmP and have successfully constructed the first PmP database in southern California. We also have delineated the Moho geometry in southern California using the PmP data together with another type of Moho-converted signals Ps from teleseismic earthquakes. Our new Moho geometry reveals a deep buried Moho beneath the northern end of the central and western Transverse Ranges. The rareness of pickable PmP waves and weak Moho-converted signals indicate the possible existence of a gradual transition from the crust to the mantle under the western Peninsular Ranges.

1. Introduction

The Moho discontinuity represents a petrological boundary separating the Earth's silicic crust from the ultramafic mantle. It is the strongest seismic discontinuity within the Earth's outermost cold shell and even within the whole solid Earth except for the core-mantle boundary. The P-wave velocity contrast across the Moho in continental region can reach ~20% in the IASP91 model (Kennett & Engdahl, 1991) or ~15% in the CM95 model (Christensen & Mooney, 1995; Rabbel et al., 2013). Thus, seismic waves derived from the Moho discontinuity, which follow the first arrivals, usually dominate the early portion of a seismogram and serve as an important toolkit to decipher crustal structures (Grad & Tiira, 2009).

Both active source surveys and passive seismic studies use Moho-related phases to constrain crustal structures. Active source surveys exploit local Moho-reflected waves PmP and Moho-refracted waves Pn (with frequency typically centered at ~10 Hz) to investigate the Moho topography and crustal volumetric structure (Grad & Tiira, 2009; Mooney, 2010; Wright et al., 2013). Passive seismic studies sometimes use local Moho-reflected waves PmP or teleseismic Moho-converted waves Ps to image the crustal structure (Figure 1). Local PmP waves

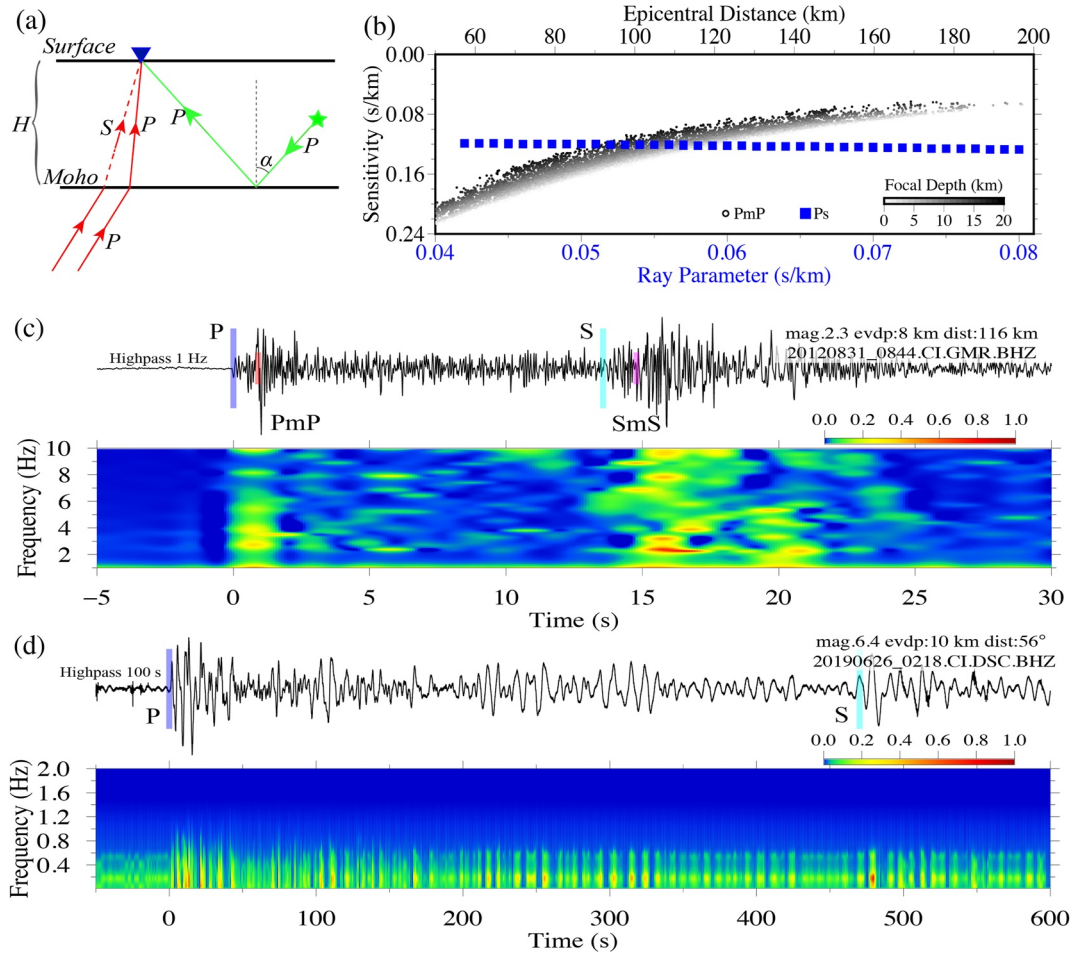

Figure 1. Comparison between the PmP and Ps waves. (a) Raypaths of local PmP wave and teleseismic P and Ps waves. The blue inverted triangle denotes a seismic station on the surface. The solid and dashed red lines show the raypaths of a teleseismic P-wave and an S-wave converted from an upgoing teleseismic P-wave (Ps), respectively. The green star denotes the seismic source that generates the local PmP wave with the raypath shown as the solid green lines. α indicates the incident angle of the local PmP wave reflected at the Moho interface, and H denotes the crustal thickness. (b) The sensitivity of the PmP travel time to the Moho depth as a function of the epicentral distance (dots gray-coded with focal depth) and that of the Ps-P differential travel time as a function of ray parameter (blue dots). The sensitivity is defined as the partial derivative of the PmP or Ps travel time with respect to the Moho depth (see the specific formulas in Text S1 in Supporting Information S1), and here they are calculated in the standard 1D P-wave velocity model for southern California (Hadley & Kanamori, 1977). The time-frequency spectrum of a seismogram generated by a near-field earthquake (c) and that of a seismogram generated by a teleseismic event (d). Both of the seismograms are recorded by broadband seismometers. The seismogram in (c) is recorded at an epicentral distance of 116 km and generated by an earthquake with magnitude 2.3 and focal depth 8.0 km, which is high-pass filtered (1 Hz) with the main four phases (P, PmP, S, and SmS) labeled. The seismogram in (d) is generated by a 56°-distant teleseismc earthquake with magnitude 6.4 and focal depth 10 km. The seismogram is high-pass filtered (100 s period).

characterized by frequency of a few hertz (typically below 6 Hz) follow alternative raypaths from first P waves and provide distinctive constraints on the lower crustal structure (Carbonell et al., 2000; Zhao, 2019). Many previous studies have attempted to pick PmP waves from local earthquakes to build crustal models (e.g., Huang et al., 2016; Nakajima et al., 2002; Richards-Dinger & Shearer, 1997; Xia et al., 2007). Receiver function (RF) analysis usually utilizes the Moho-converted signals Ps (with dominant frequency up to ~1 Hz) originating from teleseismic earthquakes to constrain the Moho depth (Ammon, 1991; Langston, 1979; Owens et al., 1984), which has greatly improved our knowledge of the Moho topography (e.g., Gilbert, 2012; Li et al., 2014).

It is preferred to jointly use local PmP waves and teleseismic Ps waves to construct the Moho topography (e.g., Hrubcová & Geissler, 2009). First, joint data sets provide us denser samplings and hence a higher imaging

resolution of the Moho geometry. Second, the different frequency contents and the distinctive raypaths through the crust between the PmP and the Ps waves together allow us to decipher the complex structures near the crust-mantle boundary (Hrubcová et al., 2013; James et al., 2003). Identifying the Moho-converted waves Ps on RFs has been done routinely (e.g., Yan & Clayton, 2007; Zhu & Kanamori, 2002). However, it is more challenging to correctly recognize the PmP waves (Sun et al., 2008). At present, the PmP waves on local seismograms are identified through either waveforms stacking (e.g., Richards-Dinger & Shearer, 1997) or phase recognition on individual traces (e.g., Nakajima et al., 2002). However, high-quality PmP waves only account for a small portion of the huge amount of recorded waveforms (e.g., ∼1%, Sun et al., 2008; Wang et al., 2018; Xia et al., 2007). It is difficult and extremely labor-intensive to search for and identify those signals manually. Therefore, an automatic or semiautomatic PmP picking workflow is definitely needed. We will develop such a workflow in this study.

Southern California, one of the most seismologically active areas in the world, is chosen as the test site (Figure 2). It has been operating one of the densest seismic networks continuously for several decades (SCEDC, 2013) and accumulated a large amount of seismic data. Studies of crustal structures in southern California have been extensively conducted, and complex Moho geometries beneath distinctive subterranes have been revealed by former studies (e.g., Mooney & Weaver, 1989; Richards-Dinger & Shearer, 1997; Yan & Clayton, 2007; Zhu & Kanamori, 2000). However, most of these studies only use one type of data to constrain the complex regional Moho geometry, with few exceptions focusing on the construction of a unified model with multiple data sets. Recently, Tape et al. (2012) constructed a smoothed Moho geometry model named the California Moho Model version 1.0 (CMM-1.0), mainly using teleseismic Moho-converted Ps data and active-source data. Since PmP waves provide complementary and importation information on the Moho geometry, in this study we attempt to use local PmP waves and teleseismic Moho-converted Ps data to image the Moho discontinuity in southern California.

We first develop a semiautomatic PmP picking workflow and apply it to the large amount of seismic waveform data accumulated in southern California in Section 2. Then, using the inversion method developed in Section 3, we construct a new Moho geometry model for southern California by jointly using the PmP and Ps data. Lastly, we investigate the discrepancies between the new Moho model and the CMM-1.0, and discuss the main factors affecting the spatial distribution of pickable PmP waves in Section 4.

2. Seismic Data

2.1. PmP Data

Previous studies have summarized the following criteria to identify PmP waves: (a) PmP waves are usually prominent on seismic waveforms of local shallow crustal earthquakes (e.g., with epicentral distance from 50 to 200 km and focal depth shallower than 20 km in southern California; Richards-Dinger & Shearer, 1997); (b) The amplitude of the PmP wave is large and sometimes larger than that of the first P, especially at postcritical epicentral distances (e.g., >70 or 80 km in the IASP91 model; Figures 3c and 3e; Bormann et al., 2012; Nakajima et al., 2002); (c) Particle motions of the PmP and P waves are similar to each other, as both are compressional waves (Figures 3b and 3d; Nakajima et al., 2002). The process of picking PmP waves can be simplified and performed in an automatic manner if we further consider: (4) there usually exists a low-amplitude zone between the P and PmP waves (Figures 3a and 4). The reliability of the picked PmP waves can be enhanced if we additionally consider: (5) Once there is a visible PmP wave from the Moho interface, it is highly possible that the SmS wave can be observed simultaneously (Figures 3a and 4; Nakajima et al., 2002). We compute synthetic waveforms in two simple crust models (Figure 3 and Figure S1 in Supporting Information S1), where the PmP waves are clearly modeled and separated from other phases. All the features aforementioned can be found in the synthetic PmP waveforms, verifying the validity of the summarized typical features of the PmP waves.

In this study, we design a two-stage process to pick PmP waves (Figure 4). At the first stage, high-quality PmP waves are picked automatically on selected seismograms. At the second stage, we expand the volume of the data set by involving other waves traveling along similar paths as those picked at the first stage.

2.1.1. Stage I: Searching for High-Quality PmP Waveforms

We pick PmP arrival times from a set of accurately located earthquakes occurring between January 2000 and December 2018 in southern California. The earthquake catalog is downloaded from the Southern California

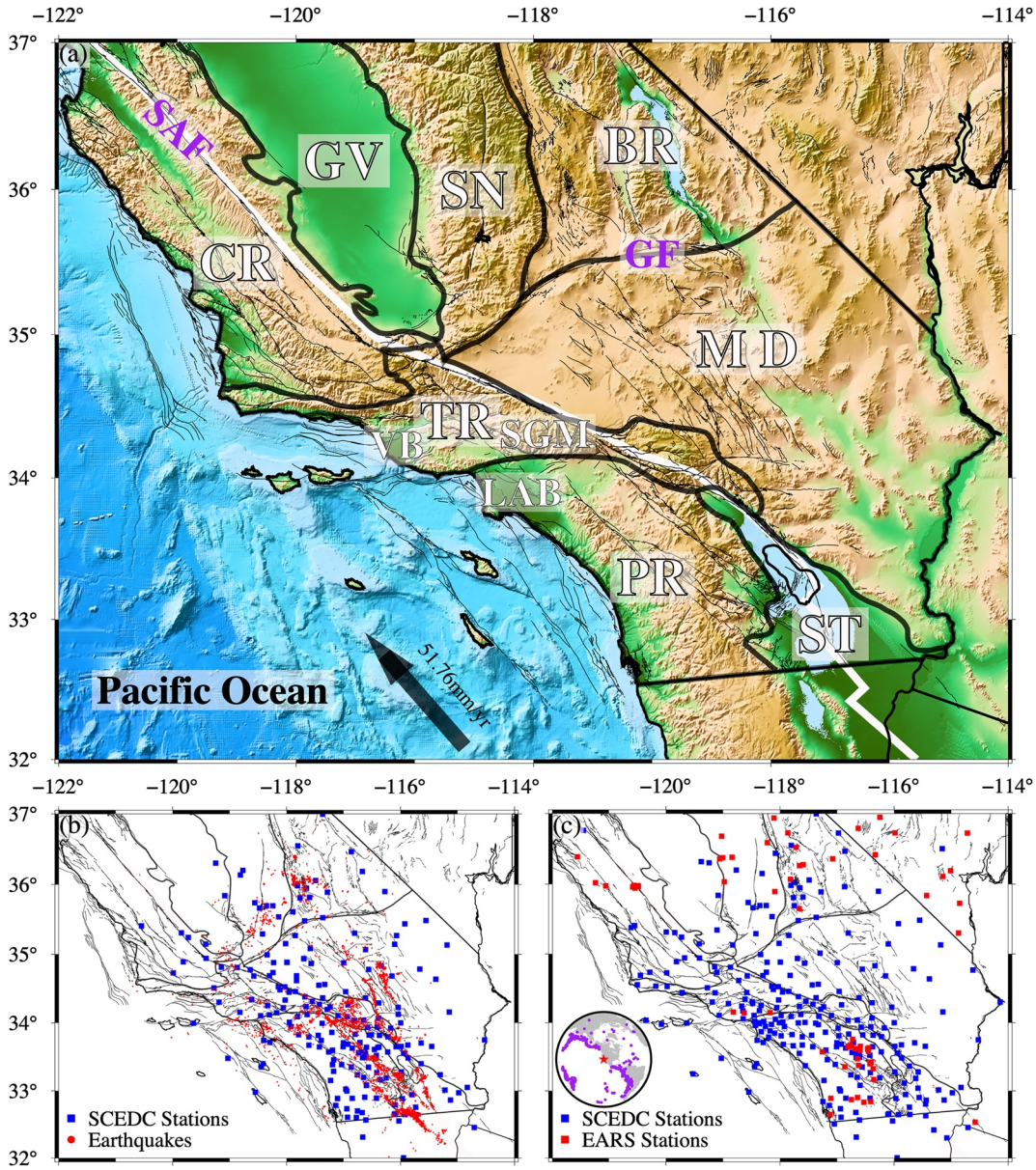

Figure 2. The tectonic settings of southern California. (a) Topography map of southern California with geologic features. Major tectonic terranes are the Great Valley (GV), Sierra Nevada (SN), Basin and Range (BR), Coast Ranges (CR), Transverse Ranges (TR), Mojave Desert (MD), Peninsular Ranges (PR), and Salton Trough (ST). Other geographical and geological features include the San Andreas Fault (SAF), the Garlock Fault (GF), the Ventura Basin (VB), the Los Angeles Basin (LAB), and the San Gabriel Mountains (SGM). The boundary between the Pacific and North American plates is denoted by the bold white line nearly coinciding with the main trace of the SAF, and the black arrow shows the relative motion between the two plates (Kreemer et al., 2014). (b) The 10,192 PmP waves picked in this study are generated by 5,838 earthquakes (red dots) and recorded by 205 seismic stations (blue squares). (c) Seismic stations chosen to do the RF analysis. Blue and red squares refer to the Southern California Earthquake Data Center (SCEDC) stations and the stations whose RF waveforms are requested from the Earth Automated Receiver Survey (EARS; Crotwell & Owens, 2005), respectively. Inset plot shows the distribution of the 803 related teleseismic earthquakes.

Seismic Network (SCSN), and a total of 21,216 earthquakes are selected based on the following two criteria: (a) The location errors are smaller than 1 and 2 km in the horizontal and vertical directions, respectively; (b) Earthquake magnitude ranges from 2.0 to 5.0 and focal depth is shallower than 20 km. Three-component seismograms of those selected earthquakes recorded at epicentral distance between 50 and 200 km are downloaded from the Southern California Earthquake Data Center (SCEDC). Then, waveforms are low-pass filtered with a cutoff

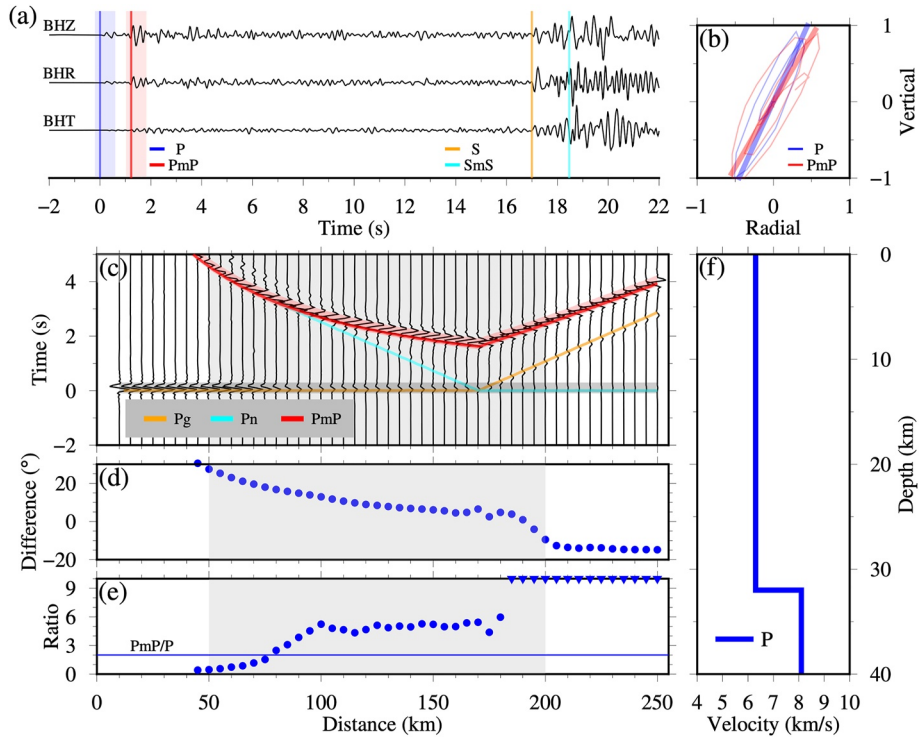

Figure 3. Typical features of local PmP waves observed on both real and synthetic waveforms. (a) A real three-component seismogram recorded at station DGR, which is generated by an earthquake with magnitude 3.0 and focal depth 5.4 km at an epicentral distance of 144 km. The onset times of main crustal phases P, PmP, S, and SmS are marked by the color-coded vertical lines. The P-wave in the blue shaded time window and the PmP wave in the red shaded time window are used to conduct the particle motion analysis. (b) The particle motions of the P-wave (blue curves) and PmP wave (pink curves) in the vertical and radial plane, along with their principal polarization directions. (c) Synthetic vertical-component seismograms computed in a one-layer crustal model shown in (f) by using the frequency-wavenumber (FK) synthetic seismogram package (Zhu & Rivera, 2002). The details of the numerical computation can be found in Text S3 in Supporting Information S1. (d) The difference in the apparent incident angles of the P and PmP waves for each synthetic trace in (c). (e) The amplitude ratio between the PmP and P waves for each synthetic trace in (c). The blue horizontal line denotes the ratio threshold we choose to automatically select the PmP waves. Note that the inverted triangles indicate that the corresponding ratio values are greater than 10.0.

frequency of 10 Hz and resampled to a uniform sampling rate of 40 Hz. A causal 4-pole Butterworth band-pass filter is further used to filter waveforms from 1 to 7 Hz, which is the main frequency range of local P and PmP waves.

There are three major steps to search for PmP waves on the band-pass filtered seismograms. The first step is to align seismic waveforms at the first P-wave arrivals. In the beginning, we measure the signal-to-noise ratio (SNR) to remove the waveforms whose first P-wave arrivals are less impulsive. The SNR of every vertical-component waveform is defined as the ratio of the peak amplitude of the signal from 2 s before to 3 s after the P-wave arrival time over the root-mean-square amplitude of the noise from 7 s before to 2 s before the P-wave arrival time. Note that the P-wave arrival times here are calculated theoretically in the standard 1D P-wave velocity model for southern California (Hadley & Kanamori, 1977; hereafter referred to as the HK model). We only retain the vertical-component waveforms with P-wave SNR greater than 10. We further determine the P-wave arrival time in the retained waveforms using the short-term average to long-term average (STA/LTA) ratio method (Trnkoczy, 1999). Following that all waveforms are aligned at the observed P-wave arrival times (see an example of aligned waveforms in Figure 4).

In the second step, PmP waves are automatically identified using a series of 1-D layered model. In detail, we construct a series of modified HK model by varying the Moho depth from 17 to 40 km with an increment of 1 km. Denoted by T_p and T_{PmP}, theoretical travel times of the P and PmP waves are computed in those models. Then, we measure the amplitude of every normalized vertical-component envelope in three nonoverlapping time windows.

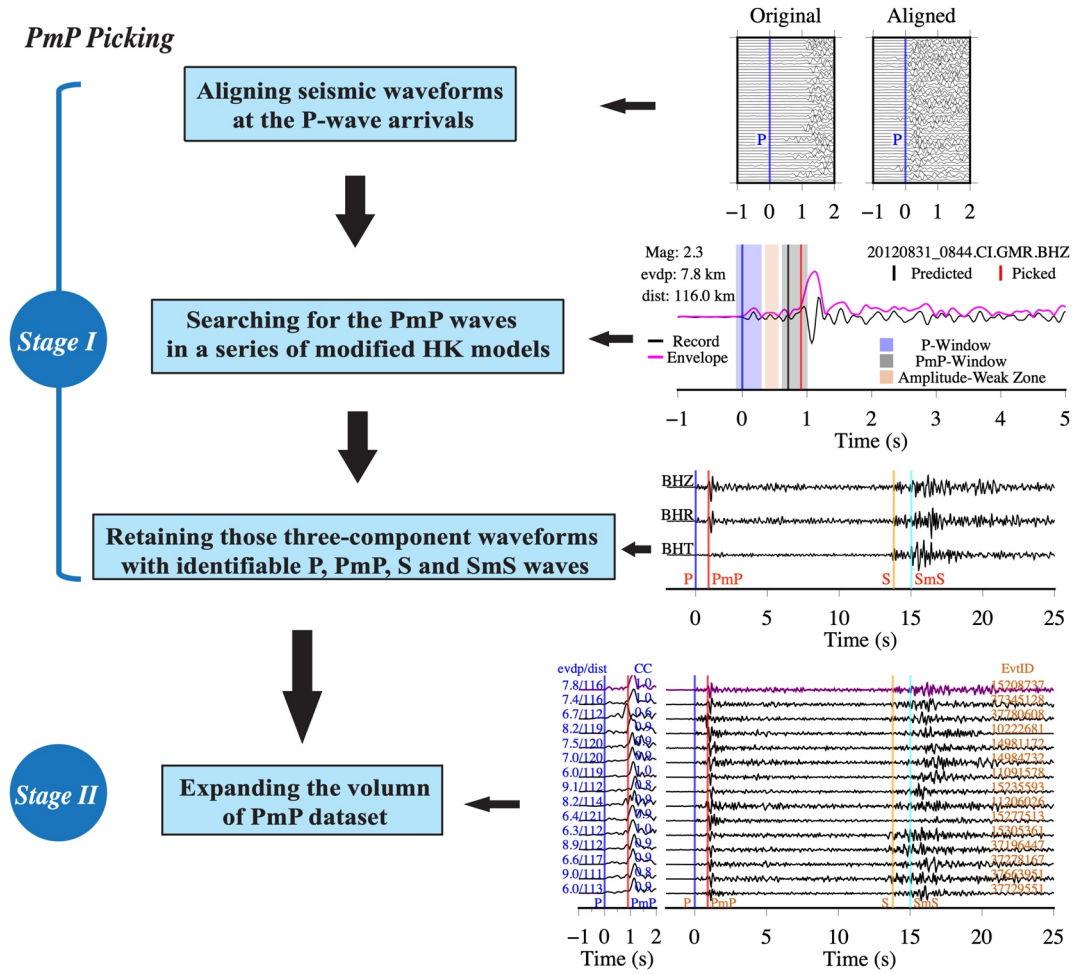

Figure 4. The two-stage process designed to pick local PmP waves with examples for each step shown on the right-hand side. Stage I includes three steps: (1) aligning the vertical-component waveforms with P-wave signal-to-noise ratio greater than 10 at the observed first P-wave arrivals. We use the STA/LTA method to automatically pick the observed P-wave arrival times; (2) automatically searching for the PmP waves based on the PmP-P differential travel time using a series of modified HK models. Waveform envelopes with a strong signal in the PmP window (in black), and a low-amplitude zone (in orange) between the P (in blue) and PmP windows are selected; and (3) retaining only those three-component waveforms with identifiable P, PmP, S, and SmS arrivals indicated by the color-coded vertical lines. Stage II attempts to expand the volume of the PmP waves picked in Stage I by assembling all the downloaded vertical-component waveforms with P-wave signal-to-noise ratio greater than 3 into common reflection gathers. We show seismic waveforms from one example gather. Each gather contains only one stage-I reference waveform (top purple trace). Earthquake depth (evdp), event-station distance (dist), and event ID (EvtID) are also listed for each trace. The waveform similarity between the only stage-I waveform and every other waveform in the same gather is checked, and we only retain those stage-II waveforms with the cross-correlation coefficient greater than 0.7.

The first time window spanning from −0.1 to 0.3 s is used to cover the first P-wave. The second time window is used to isolate the PmP wave, spanning from 0.1 s before to 0.3 s after the theoretical differential travel time between the P and PmP waves ($T_{PmP}-T_P$), which should contain the PmP wave if $T_{PmP}-T_P$ is a good approximation to the real travel time difference. The third time window is from 0.05 s after the P-wave window to 0.05 s before the PmP-wave window. If the third time window does not exist, we discard the related envelope. Finally, we regard the PmP wave as pickable only when it meets three criteria: (a) The amplitude of the PmP wave is larger than 0.7; (b) The amplitude ratio between the PmP and P waves is larger than 2 but smaller than 7; and (c) The maximum amplitude of the envelope signal in the third time window is smaller than that of the P-wave. Once a normalized envelope passes all the three criteria, it will be selected and labeled with the associated Moho depth of the modified HK model, which has been used to calculate the theoretical travel times of the P and PmP waves.

In the third step, we examine the coexistence of the PmP and SmS waves on three-component waveforms to further confirm that the identified PmP waves indeed originate from the Moho reflection. Theoretical S-P differential travel time and SmS-P differential travel time are calculated in a modified HK model with the labeled Moho depth in the second step and with the corresponding S-wave velocity based on the assumption of a Poisson solid ($V_p/V_s = 1.73$). We search for visible S and SmS waves around the two theoretical differential travel times on three-component waveforms. We only retain the waveforms with identifiable P, PmP, S, and SmS waves, and categorize the corresponding vertical-component waveforms as the stage-I waveforms.

2.1.2. Stage II: Expanding the Volume of the PmP Data Set

At the second stage, we attempt to expand the volume of the PmP data set based on waveform similarity. Previously, we only considered the vertical-component waveforms with the P-wave SNR greater than 10. Now we consider all the vertical-component waveforms with a relatively smaller P-wave SNR between 3 and 10, which are called the stage-II waveforms. Using the same procedure as the step one of the first stage, we align all the stage-II waveforms at the onset times of the P-wave arrivals. We then assemble all the stage-I and stage-II waveforms into common reflection gathers. In each gather, one waveform from the first stage is regarded as the reference waveform, and all the stage-II waveforms should have similar source locations as the reference waveform (inside a right circular cylinder with radius 10 km and height 2 km centered by the earthquake of the reference waveform) and similar receiver locations (within a distance of 10 km from the receiver of the reference waveform). After that we use a time-domain cross-correlation technique to measure the similarity between the reference waveform envelope and all the other waveform envelopes in the same gather (Schaff & Waldhauser, 2005). A time window from 2 s before to 5 s after the observed P-wave arrival is used, which is expected to include both the P and PmP waves (Figures 4 and 5g). Finally, we carefully examine and manually pick possible PmP waves from all the stage-II waveforms having cross-correlation coefficient greater than 0.7.

We further check the consistency of all the PmP travel times in each gather in an iterative way. Moho depths are estimated for all the PmP travel time data in a single gather using a constant crustal P-wave velocity of 6.3 km/s. Then, we can calculate an average Moho depth and the standard deviation for that gather. If the Moho depth estimated from an individual PmP wave deviates from the average depth by more than two times the standard deviation, the PmP wave could be an outlier and is thus excluded. The above procedure repeats until the standard deviation is less than 1 km (Figure 5h).

2.1.3. PmP Travel Time Data Set

We have picked a total of 10,192 PmP arrivals through the above two-stage PmP-picking process, including 2,462 stage-I picks and 7,730 stage-II picks. The picked PmP waveforms in different subterranes are shown in Figures S2–S6 in Supporting Information S1. To investigate the spatial distribution of the PmP data, we locate their reflection points in the HK model. As shown in Figure 5a, the western flank of the Salton Trough and the eastern Peninsular Ranges have the densest reflection points, whereas the Los Angeles Basin, the northwestern Mojave Desert, and the southern Sierra Nevada have relatively sparse data coverage. Most of the PmP waves are observed at epicentral distance from 50 to 150 km and the observed PmP travel times increase linearly with epicentral distance (Figure 5d).

We present two additional statistics, that is, the polarization difference and the amplitude ratio between the PmP and P waves, to show the reliability of the picked PmP data. First, the apparent incident angle of the P wave is measured in a time window from 0.2 s before to 0.6 s after the observed onset of the P wave, and similarly for the apparent angle of the PmP wave. The apparent incident angle is defined as the angle between the normal vector of the surface and the principal polarization direction of the particle motion in the vertical and radial plane (Wang et al., 2016). We find that most PmP waves have very similar apparent incident angles as the associated P waves, with differences less than 20° for more than 90% of the picked PmP waves (Figure 5f). The consistency in apparent incident angle indicates that the picked PmP waves polarize in the same way as the P-waves, suggesting that they are of the same type of compressional waves. Second, we compute the amplitude ratio between the PmP and P waves on the vertical-component waveforms. The ratio values concentrate around 2.5 (Figure 5e), with spatial distribution (Figure 5b) similar to that of Richards-Dinger and Shearer (1997). Large ratios (>1.65) are observed in the northern part of the Mojave Desert along the Garlock Fault, the central Mojave Desert, and the junction part between the central Transverse Ranges and the northern Peninsular Ranges. In addition, our PmP data exclusively show high amplitude ratios (>3.5) in the northern end of the central and western Transverse

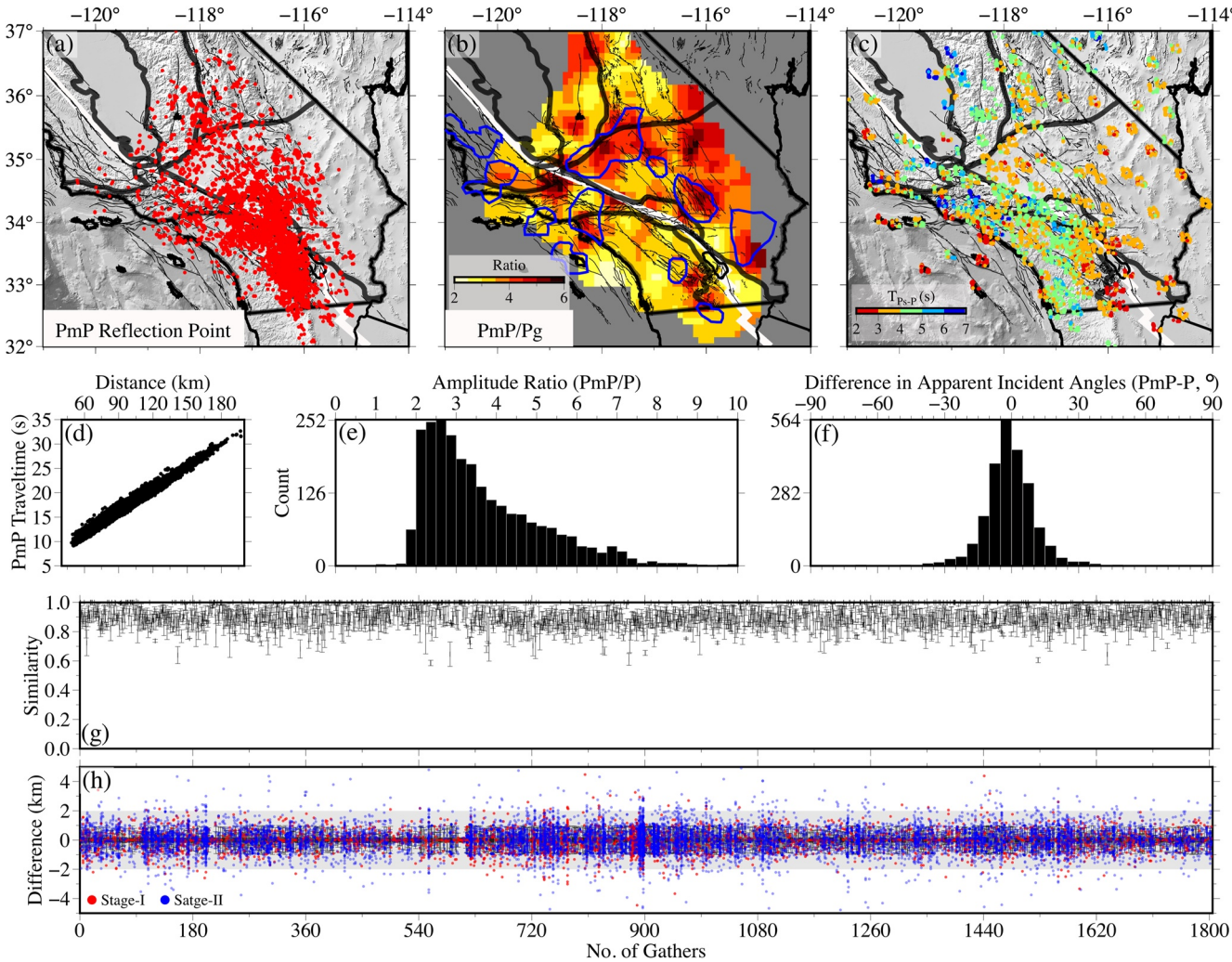

Figure 5. PmP and Ps data sets in southern California. (a) Map view of the reflection points (red dots) of all the picked PmP waves. (b) The amplitude ratio between the PmP and Pg waves. Only the ratios corresponding to stage-I waveforms are shown. The blue curves outline regions with amplitude ratio larger than 1.65 as reported by Richards-Dinger and Shearer (1997). (c) Map view of Ps conversion points color-coded with Ps-P differential travel times. (d) The correlation between PmP travel time and epicentral distance. (e) The histogram of the PmP/P amplitude ratios for stage-I waveforms. (f) The histogram of the differences between the apparent incident angles of the PmP and P waves for stage-I waveforms. (g) The average and standard deviation (vertical bars) of the cross-correlation coefficients between the reference waveform and all other waveforms in the same common reflection gather. (h) The difference between the average and each individual estimate of the Moho depth. Assuming a constant V_p = 6.3 km, each PmP wave from the same common reflection gather gives an estimate of the Moho depth. Only the PmP waves suggesting a Moho depth within ±2.0 km of the average (shaded region) are remained.

Ranges (Figure 5b and Figure S2 in Supporting Information S1). In general, a large PmP amplitude as compared to the P-wave indicates that it is a seismic phase originating from a strong seismic velocity contrast such as the Moho discontinuity (Nakajima et al., 2002).

2.2. Ps Data

Our P-wave receiver function (RF) data set includes the RFs prepared in this study and those archived by the Earth Automated Receiver Survey (EARS; Crotwell & Owens, 2005). First, we select teleseismic earthquakes occurring between January 2010 and June 2019 with epicentral distance from 30° to 90° and magnitude above 5.5 from the ANSS Comprehensive Earthquake Catalog. We download seismograms of those earthquakes recorded by 244 broadband seismic stations in southern California from SCEDC. Then, RFs are extracted by deconvolving the vertical component from the radial and transverse components with a Gaussian filter parameter of 1.5 (equivalently with central frequency around 0.75 Hz) via a time-domain iterative technique (Ligorria &

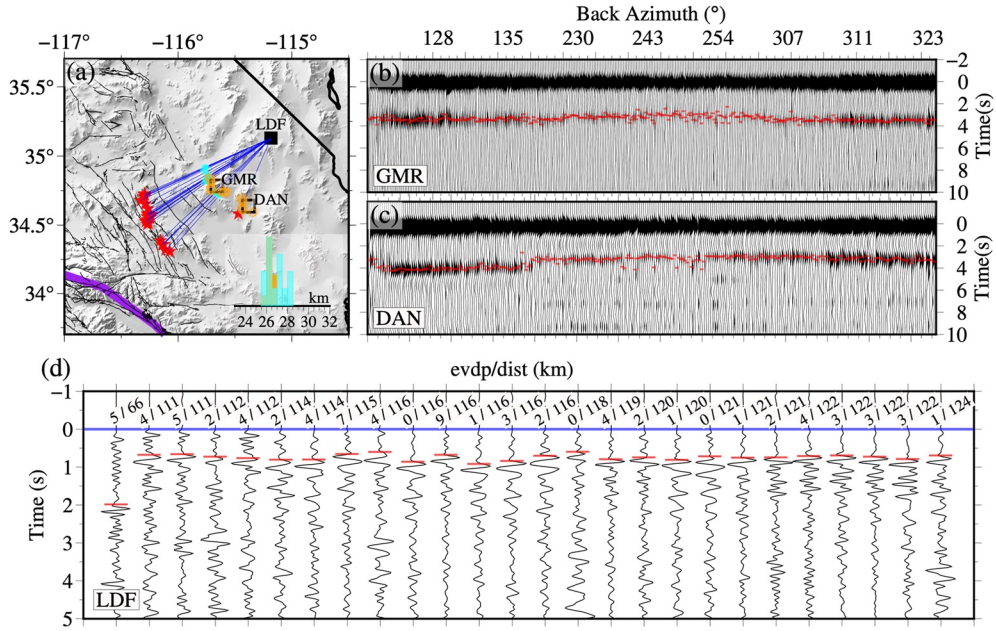

Figure 6. Ps and PmP waveforms recorded by three selected seismic stations in the Mojave Desert. (a) Map view of the example stations and earthquakes. PmP waveforms are recorded at station LDF (black square), along with the PmP reflection points shown as cyan circles. Receiver function analysis is performed at two representative stations GMR and DAN (open squares), along with the Ps conversion points indicated by the open orange circles. The inset histogram shows the PmP Moho (cyan) and the Ps Moho (orange) estimated in a one-layer crust model with V_p = 6.3 km and V_p/V_s = 1.73. (b)–(c) The receiver functions at stations GMR and DAN. Red bars indicate the picked Ps arrivals. (d) Examples of the PmP waveforms recorded at station LDF. The waveforms are aligned with the first P-wave arrivals (blue line) and sorted according to earthquake depth (evdp) and epicentral distance (dist). The PmP arrival times are indicated by the red bars.

Ammon, 1999). Moreover, we have collected RFs at 61 broadband stations from the EARS. Only high-quality RFs are retained according to two criteria: (a) The amplitude of the transverse-component P-wave is weaker than that of the radial-component; (b) The RFs are similar to each other at the same seismic station. The details of the extraction of high-quality RFs are described in Text S2 in Supporting Information S1. Finally, we obtain 38,648 high-quality RF waveforms (Figure 5c), in which 35,203 RFs are newly obtained and the other 3,445 are downloaded from the EARS.

3. Constructing the Moho Geometry Using the Ps and PmP Data

Both the PmP and Ps waves are sensitive indicators that can help us constrain the Moho geometry (Figure 6 and Figure S7 in Supporting Information S1). *H*-κ stacking is a routine technique to determine Moho depth (*H*) and bulk velocity ratio (*Vp/Vs* or κ) using the P-wave RFs (Zhu & Kanamori, 2000). This technique works well when seismic stations situate above a simple crust. However, when seismic stations situate above a relatively complex crust, the Moho-related multiples could be mingled with other intracrust-generated signals, resulting in ambiguity in the estimation of Moho depth and bulk velocity ratio (Figure S8 in Supporting Information S1). In this study, to account for crustal velocity heterogeneities, we first construct the Moho geometry beneath southern California in the 3D community velocity model CVM-S4.26 (Lee et al., 2014; hereafter referred to as the CVM-S model) by applying the common conversion point (CCP) stacking technique (Zhu, 2000; Xu et al., 2020) to P-wave RFs. We call the Moho geometry constrained by the Ps data as the Ps Moho. Then, we further update the Ps Moho by inverting PmP travel time data in the 3D community velocity model CVM-H15.1.1 (Shaw et al., 2015; hereafter referred to as the CVM-H model).

3.1. Using CCP Stacking Technique to Construct the Ps Moho

A P-wave RF is a time series consisting of a direct P arrival and P-to-S converted pulses generated by underground discontinuities along the receiver-side propagation path (Bostock, 2015). The locations of those discontinuities

can be determined by migration techniques. In this study, we use the common conversion point (CCP) stacking method to image the Moho discontinuity (Zhu, 2000; Xu et al., 2020). The success of CCP stacking relies on the accuracy of the velocity model in which the time-to-depth mapping is performed. Thus, before the CCP stacking we build a reliable 3D velocity model by combining the 3D community velocity model CVM-S with the upper mantle part of the IASP91 model.

First, the RFs recorded at every single station are projected to the depth domain, based on the 1D velocity profile beneath that station extracted from the 3D velocity model. Here, the locations of converted S-wave piercing points are computed in the depth domain ranging from the surface to 100 km at a vertical interval of 0.5 km. Then, we generate bins around regularly spaced nodes with intervals of 15 km, 15 km, and 0.5 km in the longitude, latitude, and depth directions, respectively. Centered at every node, CCP stacking is performed by binning those amplitude-varying piercing points. All bins have a uniform width of 30 km. Up to now, we have obtained a 3D CCP stacking image of southern California. The Moho depth is subsequently searched in a range that is 10 km below and 10 km above the CMM-1.0 by locating the positive maximum amplitude of the CCP stacking image. After that we visually check the amplitudes of the CCP stacking image at places where the Moho depth estimates deviate largely from the reference CMM-1.0 (Figure S9 in Supporting Information S1). For instance, we consider that the positive signals at a deeper depth in the CCP stacking image beneath the eastern Great Valley and the western Sierra Nevada are related to the Moho discontinuity (Figure S10b in Supporting Information S1), because these signals are stronger and a deep Moho (~55 km) has been reported by former regional RF analyses (Frassetto et al., 2011). Similarly beneath the southern Basin and Range and the northern Mojave Desert, the deeper positive signals are considered to be related to the Moho, as the inferred Moho is consistent with the Moho geometry in nearby regions (Figure S10c in Supporting Information S1). Regarding the local deep Moho beneath the eastern Mojave Desert (Figure S10d in Supporting Information S1), because it deviates largely from the nearby Ps Moho geometry and former studies (Zhu & Kanamori, 2000; Yan & Clayton, 2007), we remove it from our Moho model. Near the boundaries, no Ps data are available to constrain the Moho topography. We directly use the estimates of the CMM-1.0 to fill in those gaps (Figure S11e in Supporting Information S1). The obtained Moho for the entire southern California is further smoothed by convolving it with a 2D Gaussian function, whose full width at half maximum is 71.2 km (Figure S11f in Supporting Information S1). For convenience, the smoothed Moho is called the Ps Moho.

3.2. Using the PmP Travel Time Data to Update the Ps Moho

The PmP travel time data are inverted to improve the accuracy of the Ps Moho. As is known, a precise crustal P-wave velocity model is essential for the accurate determination of the Moho depth using PmP arrival times. The 3D community velocity model CVM-H, which includes basin structures and the adjoint tomography (waveform inversion) model of Tape et al. (2009), maintains a high level of accuracy in representing crustal P-wave velocity heterogeneities. So, we choose to update the Ps Moho in the CVM-H model by inverting PmP arrival times. It is worth noting that earthquake locations also affect the accuracy of Moho depth derived from PmP data. To reduce the influence to a low limit, the locations of all the associated earthquakes are revised according to the HYS_catalog_2011 (Hauksson et al., 2012), where most earthquakes have location errors less than 0.75 km horizontally and 1.25 km in the depth direction.

Initially, we embed the Ps Moho in the 3D CVM-H model with the necessary extension or shortening of the lower crustal structure (Figure S12 in Supporting Information S1). Then, we trace the raypaths of PmP waves in that model. In detail, for every PmP wave, the travel time field from the earthquake location and the travel time field initiated at the receiver location are computed by numerically solving the eikonal equation twice, and the reflection point is found by locating the minimum sum of the time from the earthquake to the Moho and the time from the receiver to the Moho; starting at the reflection point, the two legs of the PmP raypath are traced along the negative gradients of the two travel time fields. Following Nakjima et al. (2002), the misfit between the observed PmP arrival time T_{obs} and the calculated travel time T_{cal} suggests a necessary correction $\Delta d(\boldsymbol{x}_r)$ of the Moho depth at the reflection point $\boldsymbol{x}_r$. Mathematically, this relationship can be expressed by

$$T_{obs} - T_{cal} = \frac{2\ \cos\ \theta}{v\left(\boldsymbol{x}_r\right)} \Delta d\left(\boldsymbol{x}_r\right), \tag{1}$$

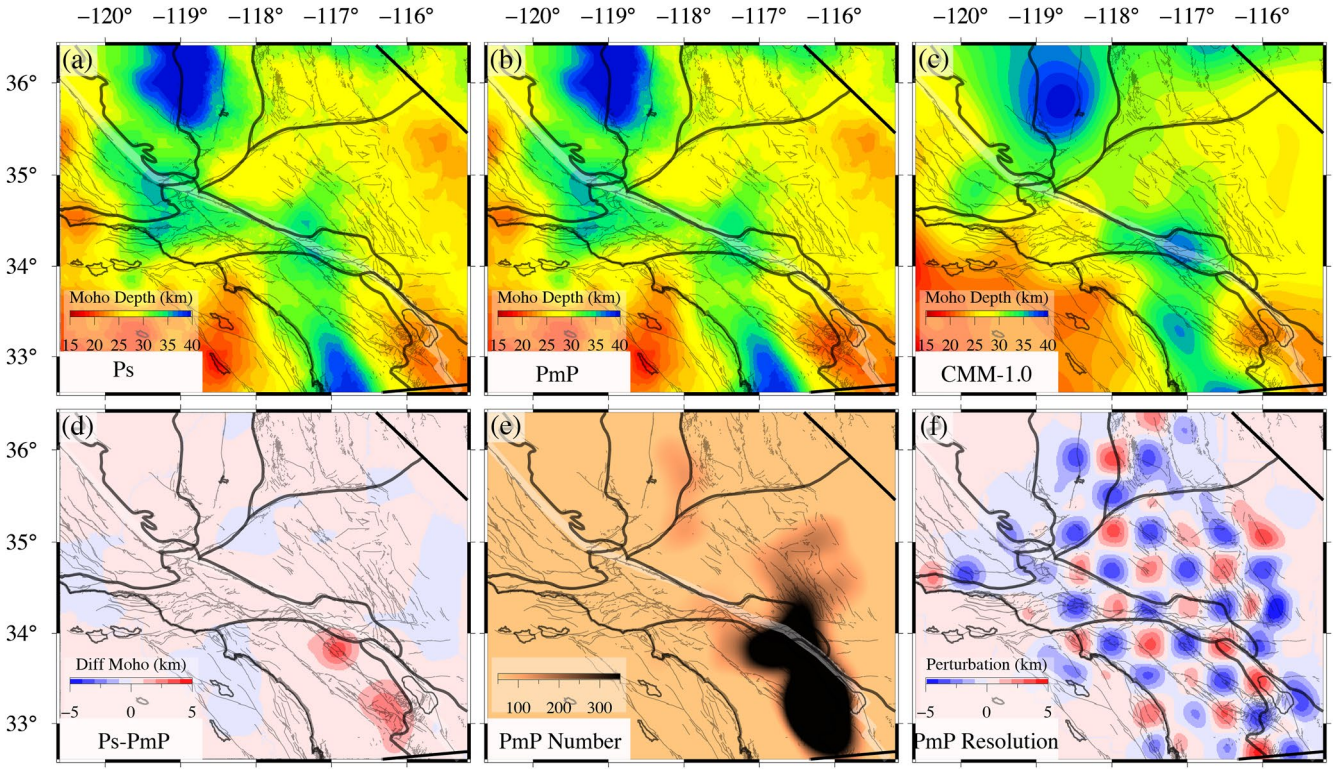

Figure 7. Moho models for southern California. (a) Moho geometry extracted from the 3D common conversion point stacking image. (b) The updated Moho geometry obtained by inverting the PmP travel times. (c) Moho geometry of the CMM–1.0. (d) The difference between the Ps Moho and our final Moho model. (e) The count of PmP reflection points. (f) Checkboard resolution test showing the ability of the PmP travel time data in resolving Moho undulations.

where θ is the reflection angle of the PmP wave and $v(\boldsymbol{x}_r)$ is the P-wave speed at $\boldsymbol{x}_r$. After tracing the raypaths of all the PmP waves and discretizing the Moho perturbation $\Delta d(\boldsymbol{x}_r)$ with the multiple-grid approach (Tong et al., 2019), we formulate a large linear system of $\boldsymbol{Gm} = \boldsymbol{d}$, which is solved by the LSQR solver (Paige & Sanders, 1982). The Moho depth is iteratively updated. Given the high accuracy of the initial Ps Moho, the deviation of each updated Moho from the Ps Moho is restricted within ±5 km by setting a proper damping parameter during the inversion. A stable solution is obtained after 16 iterations. As shown in Figure 7, the updated Moho has the same pattern as the Ps Moho. The main differences lie beneath the western flank of the Salton Trough and the northeastern Peninsular Ranges, where the PmP data indicate a 2.5-km shallower Moho (Figure 7d). As the chosen PmP data densely sample these two areas (Figure 7e) and in addition, the checkboard resolution test suggests that Moho undulations with a size of 30 km in almost all the onshore regions can be well resolved (Figure 7f), we believe that the new features revealed by the PmP data are reliable. We thus take the updated Moho geometry as our final Moho model for southern California.

3.3. Moho Geometry in Southern California

We have constructed a new Moho geometry model for southern California based on the joint PmP and Ps data sets. Our Moho model has overall similar patterns to the previous CMM-1.0 (Figures 7a–7c, Figure S13 in Supporting Information S1), for example, the Salton Trough and its adjacent western flank have the shallowest Moho (23 km), the Peninsular Ranges has an eastward shallowing Moho, the Mojave Desert situates above a uniformly shallow Moho (27 km), and the Moho beneath the Transverse Ranges is slightly deep (31 km) in general. To the north of the Garlock Fault, the Moho is deep under the Great Valley and the Sierra Nevada (34 km), whereas a relatively shallow Moho is observed beneath the Basin and Range (29 km). However, in comparison with the CMM-1.0, our new Moho map shows a deeper Moho beneath the western Sierra Nevada (40 km) and the northern end of the central and western Transverse Ranges (34 km), whereas a slightly shallower Moho under the Basin and Range.

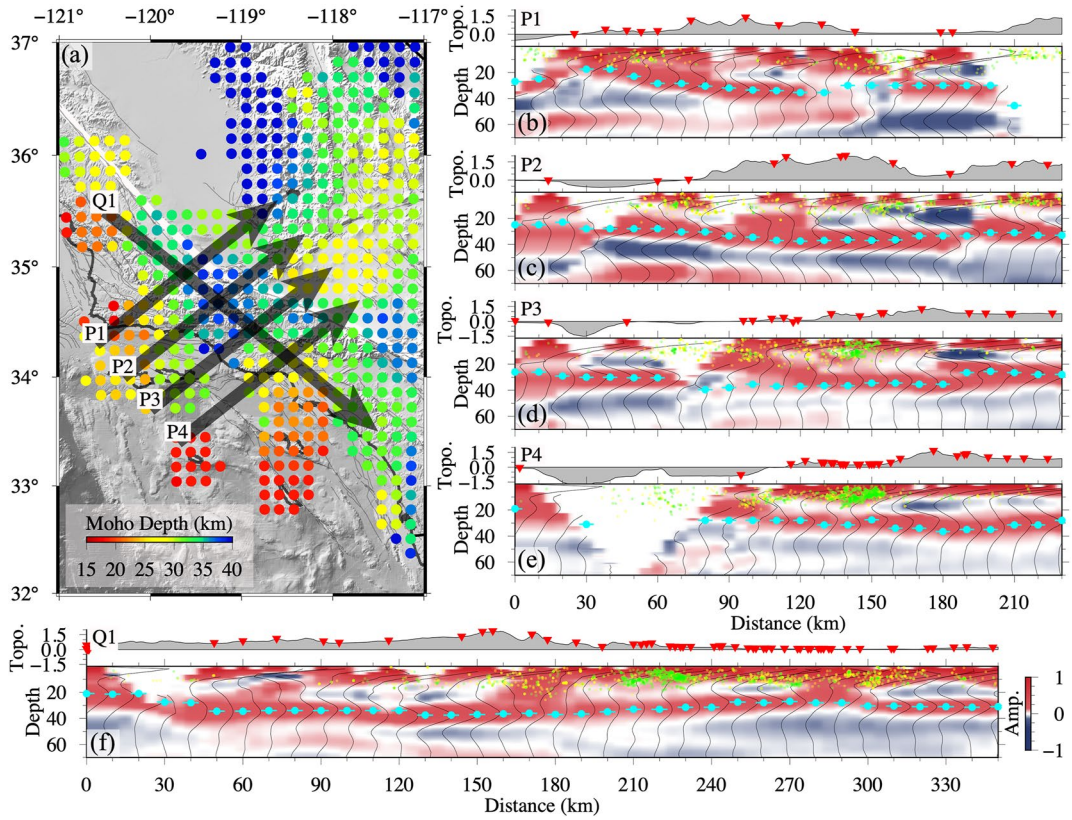

Figure 8. 2D CCP stacking images beneath the central-western Transverse Ranges. (a) The Ps Moho and locations of five profiles. (b) The common conversion point (CCP) stacking image along profile P1. In the upper panel, we show the surface topography and seismic stations along the profile (within 30 km). In the lower panel, the CCP stacked P-to-S amplitudes have been smoothed in the Fresnel zone. Red and blue colors indicate that the velocity increases and decreases with depth, respectively. Cyan dots follow the estimated geometry of the Ps Moho. Earthquakes occurring within 30 km from the profile are projected onto the image. Yellow dots show earthquakes with magnitude greater than 2.0 occurring during the period from 2008 to 2017 from Ross et al. (2019). Green dots show earthquakes with magnitude greater than 3.0 occurring during the period from 1981 to 2020 from Hauksson et al. (2012). (c)–(f) The CCP stacking images along other profiles.

4. Discussion

4.1. Discrepancies Between the Newly Updated Moho and the CMM-1.0

Our Moho model reveals a deep Moho (>40 km) beneath the western Sierra Nevada, which correlates well with the dense mafic-ultramafic residue beneath the western Sierra Nevada batholith (Frassetto et al., 2011; Levandowski & Jones, 2015). Although the CMM-1.0 shows a similar deep Moho in the same region, the Moho in our model is deeper and the deepest site locates farther west (Figures 7b and 7c). Meanwhile, in the Basin and Range, the updated Moho is slightly shallower than the CMM-1.0, probably related to the fact that the CVM-H model involves considerable lower-crustal low-velocity anomalies in this region.

There is a pronounced difference between our new Moho model and the CMM-1.0 beneath the northern end of the central and western Transverse Ranges (Figures 7b and 7c). The CMM-1.0 shows a generally shallower Moho in this region (27 km), whereas our model points to a deeper Moho of about 34 km. The elusive Moho depth beneath the central and western Transverse Ranges has long been a controversial topic, which is probably associated with the complex crustal structures. For example, between 70 and 120 km along the profile shown in Figure 8d, we observe two positive P-to-S signals around the regional averaged Moho depth. In addition, Yan and Clayton (2007) reported that RFs sampling the central and westernmost Transverse Ranges are rather complicated, and the Moho depth inferred from RFs at several stations may reach 39 km beneath the western San Gabriel Mountains in the central Transverse Ranges. We consider that the deeper positive P-to-S signal is related to the Ps Moho as it coincides with the deep Moho to the east. Earlier study analyzing local earthquake travel time

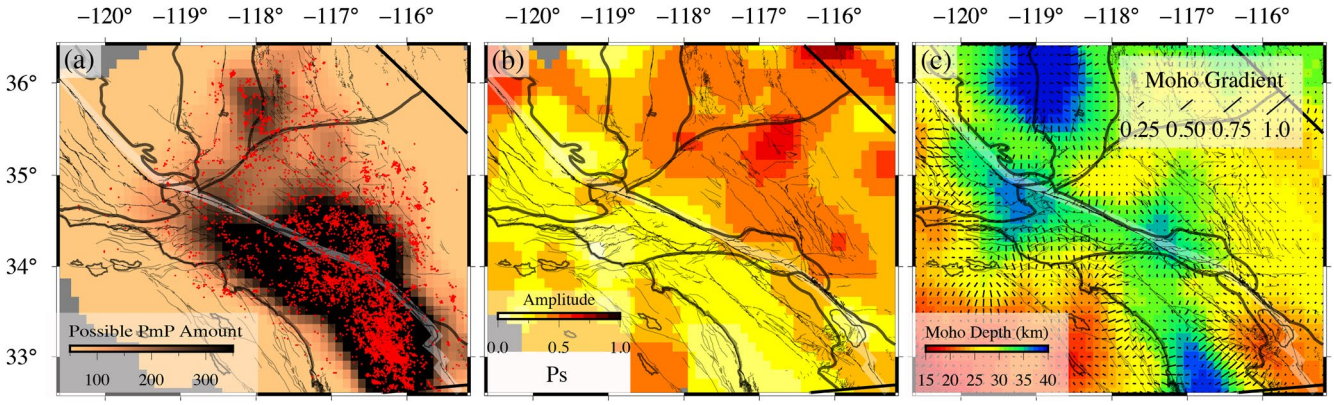

Figure 9. (a) Density of waveforms that possibly contain identifiable PmP waves (color-coded in copper). Red dots show the reflection points of those picked PmP waves. (b) The normalized amplitude of the Ps phase in the 3D common conversion point stacking image. (c) The gradient of our final Moho model. The black bars refer to the direction along which the Moho geometry changes the fastest, and the lengths of black bars (slope) have been normalized.

curves of Bryant and Jones (1992), PmP stacking data of Richards-Dinger and Shearer (1997), and CCP stacking image along the Los Angeles Region Seismic Experiments (LARSE-II, Zhu, 2002) also suggest a deep Moho (more than 35 km) in this region. We find that the deep Moho beneath the westernmost San Gabriel Mountains and the northwestern Ventura Basin coincides with the area of low heat flow (Shinevar et al., 2018) and deep crustal seismicity (down to 20 km depth, Figure 8), suggesting the existence of a thick brittle seismogenic layer (Shinevar et al., 2018).

4.2. Rareness of Pickable PmP Waves in the Western Peninsular Ranges

Active source surveys suggest that the Moho is a complex transition zone of finite thickness between the crust and the mantle rather than a simple sharp velocity discontinuity (Jarchow & Thompson, 1989). The transition zone from the crust to the mantle is generally 0–3 km thick in oceanic regions or 0–5 km thick in continental regions (Braile & Chiang, 1986). The amplitude of the Moho-converted Ps wave is a sensitive indicator of the Moho sharpness (Youssof et al., 2013). We extract and normalize the amplitude of the binned Ps waves from the 3D CCP stacking image at Moho depth (Figure 9b). The average Ps amplitude in our study region is 0.34. Specifically, the amplitudes of Ps waves are large beneath the eastern Peninsular Ranges, the northern end of the central and western Transverse Ranges (>0.3), and are even larger than 0.4 along the Garlock Fault and in the Mojave Desert. These patterns coincide well with the PmP/Pg amplitude ratios (Figure 5b). On the contrary, the Ps waves in the western Peninsular Ranges and the central-western Transverse Ranges are rather weak (0.2), suggesting the possible existence of a gradual crust-mantle transition zone there.

In the western Peninsular Ranges, few PmP waves are detected, which was also reported by Richards-Dinger and Shearer (1997). Although the amount of waveforms with P-wave SNR>3 possibly containing identifiable PmP waves in the western Peninsular Ranges is comparable to that in the eastern Mojave Desert, we are unable to identify the same amount of reliable PmP waves in the western Peninsular Ranges as in the eastern Mojave Desert. We observe that the Moho geometry changes rapidly across the Peninsular Ranges in the west-east direction (Figure 9c), and the middle segment of the Moho transitioning from the western Peninsular Ranges toward its eastern counterpart has the steepest slope. The amount of picked PmP waves in the transition zone is much lesser than expected. This is probably caused by the dipping geometry of the Moho, as PmP waves tend to be reflected at the eastern shallower parts. However, the Moho is flat in the western Peninsular Ranges, suggesting that the rareness of the pickable PmP waves is unlikely due to the dipping Moho. Here, we propose that the small amount of pickable PmP waves in the western Peninsular Ranges is likely related to the gradual transition between the lower crust and the uppermost mantle, where both the PmP/Pg ratio and Ps signals are weak (Figures 5b and 9b). The model of Barak et al. (2015) also demonstrates such a gradual transition, in which the lower crustal shear-wave velocity is only slightly smaller than that in the uppermost mantle.

5. Conclusions

In this study we have developed a semiautomatic process to pick seismic reflected waves PmP on raw seismograms. The newly developed process has been applied to analyzing a large amount of seismic data in southern California. As a result, we have successfully identified a total of 10,192 high-quality PmP waves and picked their arrival times.

We have updated the Moho geometry model of southern California by jointly using the Ps and PmP data. The newly updated Moho geometry shows similar patterns with previous results, such as the well compiled CMM-1.0. The crust is generally thin beneath the Salton Trough (23 km), the Mojave Desert, and the Basin and Ranges (<29 km); whereas a deep Moho is observed beneath the western Peninsular Ranges, the Transverse Ranges, the Great Valley, and the western Sierra Nevada (>33 km). Strikingly different from the CMM-1.0, our new Moho model indicates a rather deep Moho beneath the northern end of the central and western Transverse Ranges, where a thick brittle seismogenic zone exists as revealed by the deep local seismicity.

The valuable PmP data can increase the illumination of the lower crustal structure and the Moho topography. The entire crustal structure can be well delineated by jointly using the P- and PmP waves, bearing a great potential for improving our understanding of crustal deformations and geodynamic processes. To accommodate massive amounts of seismic data and the rapid proliferation in the future, developing an effective machine learning method is promising to considerably reduce toil (Kong et al., 2018). In this regard, the PmP data picked in the present study can serve as a benchmark data set to build a specific PmP-identifying machine learning model, which could be used to routinely process continuously increasing seismic data in southern California and other regions.

Data Availability Statement

The seismic data and local earthquake catalog are requested from Southern California Earthquake Data Center (https://scedc.caltech.edu/). The ANSS Comprehensive Earthquake Catalog is provided by the U.S. Geological Survey (https://earthquake.usgs.gov/data/comcat/). Receiver function waveforms from the Earth Automated Receiver Survey are requested at http://ds.iris.edu/ds/products/ears/ (last accessed time 22 Oct 2019). The picked PmP travel times and the Moho topography models in this study can be accessed at https://doi.org/10.21979/N9/HKCXBF.

Acknowledgments
The authors are grateful to Editor Michael Bostock, an associate editor and two anonymous reviewers for their constructive comments. This work comprises Earth Observatory of Singapore contribution no. 368. This research is partly funded by the National Research Foundation Singapore and the Singapore Ministry of Education under the Research Centers of Excellence Initiative (Project Code Number: 04MNS001953A620). T. Li and P. Tong are also partly supported by Singapore MOE AcRF Tier-2 Grant (04MNP002073C230). Figures are made with GMT (Wessel & Smith, 1998). TauP Toolkit (Crotwell et al., 1999) is used when calculating the theoretical travel times and raypaths of seismic phases in synthetic tests. Seispy (https://seispy.xumijian.me/) is used to conduct the CCP stacking.

References

Ammon, C. J. (1991). The isolation of receiver effects from teleseismic P waveforms. *Bulletin of the Seismological Society of America*, *81*(6), 2504–2510. https://doi.org/10.1785/bssa0810062504

Barak, S., Klemperer, S. L., & Lawrence, J. F. (2015). San Andreas Fault dip, Peninsular Ranges mafic lower crust and partial melt in the Salton Trough, Southern California, from ambient-noise tomography. *Geochemistry, Geophysics, Geosystems*, *16*(11), 3946–3972. https://doi.org/10.1002/2015gc005970

Bormann, P., Engdahl, B., & Kind, R. (2012). Seismic wave propagation and earth models. *New manual of seismological observatory practice*, *2*, 1–105.

Bostock, M. G. (2015). Theory and observations - Seismology and the structure of the earth: Teleseismic body-wave scattering and receiver-side structure. In *Treatise on geophysics* (pp. 253–275). https://doi.org/10.1016/b978-0-444-53802-4.00008-7

Braile, L., & Chiang, C. (1986). The continental Mohorovičić discontinuity: Results from near-vertical and wide-angle seismic reflection studies. *Reflection seismology: A global perspective*, *13*, 257–272. https://doi.org/10.1029/gd013p0257

Bryant, A. S., & Jones, L. M. (1992). Anomalously deep crustal earthquakes in the Ventura basin, southern California. *Journal of Geophysical Research*, *97*(B1), 437–447. https://doi.org/10.1029/91jb02286

Carbonell, R., Gallart, J., Pérez-Estaún, A., Diaz, J., Kashubin, S., Mechie, J., et al. (2000). Seismic wide-angle constraints on the crust of the southern Urals. *Journal of Geophysical Research*, *105*(B6), 13755–13777. https://doi.org/10.1029/2000jb900048

Christensen, N. I., & Mooney, W. D. (1995). Seismic velocity structure and composition of the continental crust: A global view. *Journal of Geophysical Research*, *100*(B6), 9761–9788. https://doi.org/10.1029/95jb00259

Crotwell, H. P., & Owens, T. J. (2005). Automated receiver function processing. *Seismological Research Letters*, *76*(6), 702–709. https://doi.org/10.1785/gssrl.76.6.702

Crotwell, H. P., Owens, T. J., & Ritsema, J. (1999). The TauP Toolkit: Flexible seismic travel-time and ray-path utilities. *Seismological Research Letters*, *70*(2), 154–160. https://doi.org/10.1785/gssrl.70.2.154

Frassetto, A. M., Zandt, G., Gilbert, H., Owens, T. J., & Jones, C. H. (2011). Structure of the Sierra Nevada from receiver functions and implications for lithospheric foundering. *Geosphere*, *7*(4), 898–921. https://doi.org/10.1130/ges00570.1

Gilbert, H. (2012). Crustal structure and signatures of recent tectonism as influenced by ancient terranes in the western United States. *Geosphere*, *8*(1), 141–157. https://doi.org/10.1130/ges00720.1

Grad, M., & Tiira, T. (2009). The Moho depth map of the European Plate. *Geophysical Journal International*, *176*(1), 279–292. https://doi.org/10.1111/j.1365-246x.2008.03919.x

Hadley, D., & Kanamori, H. (1977). Seismic structure of the transverse ranges, California. The *Geological Society of America Bulletin*, *88*(10), 1469–1478. https://doi.org/10.1130/0016-7606(1977)88<1469:ssottr>2.0.co;2

Hauksson, E., Yang, W., & Shearer, P. M. (2012). Waveform relocated earthquake catalog for southern California (1981 to June 2011). *Bulletin of the Seismological Society of America*, *102*(5), 2239–2244. https://doi.org/10.1785/0120120010
Hrubcová, P., & Geissler, W. H. (2009). The crust-mantle transition and the Moho beneath the Vogtland/West Bohemian region in the light of different seismic methods. *Studia Geophysica et Geodaetica*, *53*(3), 275–294.
Hrubcová, P., Vavryčuk, V., Boušková, A., & Horálek, J. (2013). Moho depth determination from waveforms of microearthquakes in the West Bohemia/Vogtland swarm area. *Journal of Geophysical Research: Solid Earth*, *118*(1), 120–137.
Huang, X., Yang, D., Tong, P., Badal, J., & Liu, Q. (2016). Wave equation-based reflection tomography of the 1992 Landers earthquake area. *Geophysical Research Letters*, *43*(5), 1884–1892. https://doi.org/10.1002/2016gl067717
James, D. E., Niu, F., & Rokosky, J. (2003). Crustal structure of the Kaapvaal craton and its significance for early crustal evolution. *Lithos*, *71*(2–4), 413–429. https://doi.org/10.1016/j.lithos.2003.07.009
Jarchow, C. M., & Thompson, G. A. (1989). The nature of the Mohorovicic discontinuity. *Annual Review of Earth and Planetary Sciences*, *17*(1), 475–506. https://doi.org/10.1146/annurev.ea.17.050189.002355
Kennett, B., & Engdahl, E. (1991). Traveltimes for global earthquake location and phase identification. *Geophysical Journal International*, *105*(2), 429–465. https://doi.org/10.1111/j.1365-246x.1991.tb06724.x
Kong, Q., Trugman, D. T., Ross, Z. E., Bianco, M. J., Meade, B. J., & Gerstoft, P. (2018). Machine learning in Seismology: Turning data into insights. *Seismological Research Letters*, *90*(1), 3–14. https://doi.org/10.1785/0220180259
Kreemer, C., Blewitt, G., & Klein, E. C. (2014). A geodetic plate motion and global strain rate model. *Geochemistry, Geophysics, Geosystems*, *15*(10), 3849–3889. https://doi.org/10.1002/2014gc005407
Langston, C. A. (1979). Structure under Mount Rainier, Washington, inferred from teleseismic body waves. *Journal of Geophysical Research: Solid Earth*, *84*(B9), 4749–4762. https://doi.org/10.1029/jb084ib09p04749
Lee, E. J., Chen, P., Jordan, T. H., Maechling, P. B., Denolle, M. A. M., & Beroza, G. C. (2014). Full-3-D tomography for crustal structure in Southern California based on the scattering-integral and the adjoint-wavefield methods. *Journal of Geophysical Research: Solid Earth*, *119*(8), 6421–6451. https://doi.org/10.1002/2014jb011346
Levandowski, W., & Jones, C. H. (2015). Linking Sierra Nevada, California, uplift to subsidence of the Tulare basin using a seismically derived density model. *Tectonics*, *34*(11), 2349–2358. https://doi.org/10.1002/2015tc003824
Li, Y., Gao, M., & Wu, Q. (2014). Crustal thickness map of the Chinese mainland from teleseismic receiver functions. *Tectonophysics*, *611*, 51–60. https://doi.org/10.1016/j.tecto.2013.11.019
Ligorria, J. P., & Ammon, C. J. (1999). Iterative deconvolution and receiver-function estimation. *Bulletin of the Seismological Society of America*, *89*(5), 1395–1400. https://doi.org/10.1785/bssa0890051395
Mooney, W. D. (2010). Crust and lithospheric structure–global crustal structure. *Seismology and Structure of the Earth: Treatise on Geophysics*, *1*, 361.
Mooney, W. D., & Weaver, C. S. (1989). Regional crustal structure and tectonics of the Pacific coastal states; California, Oregon, and Washington. *Geophysical framework of the continental United States*, *172*, 129–161. https://doi.org/10.1130/mem172-p129
Nakajima, J., Matsuzawa, T., & Hasegawa, A. (2002). Moho depth variation in the central part of northeastern Japan estimated from reflected and converted waves. *Physics of the Earth and Planetary Interiors*, *130*(1–2), 31–47. https://doi.org/10.1016/s0031-9201(01)00307-7
Owens, T. J., Zandt, G., & Taylor, S. R. (1984). Seismic evidence for an ancient rift beneath the Cumberland Plateau, Tennessee: A detailed analysis of broadband teleseismic P waveforms. *Journal of Geophysical Research*, *89*(B9), 7783–7795. https://doi.org/10.1029/jb089ib09p07783
Paige, C., & Sanders, M. A. (1982). LSQR: An algorithm for sparse linear equation and sparse least squares. *ACM Transactions on Mathematical Software*, *8*, 43–71. https://doi.org/10.1145/355984.355989
Rabbel, W., Kaban, M., & Tesauro, M. (2013). Contrasts of seismic velocity, density and strength across the Moho. *Tectonophysics*, *609*, 437–455. https://doi.org/10.1016/j.tecto.2013.06.020
Richards-Dinger, K. B., & Shearer, P. M. (1997). Estimating crustal thickness in southern California by stackingPmParrivals. *Journal of Geophysical Research*, *102*(B7), 15211–15224. https://doi.org/10.1029/97jb00883
Ross, Z. E., Trugman, D. T., Hauksson, E., & Shearer, P. M. (2019). Searching for hidden earthquakes in Southern California. *Science*, *364*(6442), 767–771. https://doi.org/10.1126/science.aaw6888
SCEDC. (2013). *Southern California earthquake data center*. Caltech. Dataset.
Schaff, D. P., & Waldhauser, F. (2005). Waveform cross-correlation-based differential travel-time measurements at the Northern California Seismic Network. *Bulletin of the Seismological Society of America*, *95*(6), 2446–2461. https://doi.org/10.1785/0120040221
Shaw, J. H., Plesch, A., Tape, C., Suess, M. P., Jordan, T. H., Ely, G., et al. (2015). Unified Structural Representation of the southern California crust and upper mantle. *Earth and Planetary Science Letters*, *415*, 1–15. https://doi.org/10.1016/j.epsl.2015.01.016
Shinevar, W. J., Behn, M. D., Hirth, G., & Jagoutz, O. (2018). Inferring crustal viscosity from seismic velocity: Application to the lower crust of Southern California. *Earth and Planetary Science Letters*, *494*, 83–91. https://doi.org/10.1016/j.epsl.2018.04.055
Sun, A., Zhao, D., Ikeda, M., Chen, Y., & Chen, Q. (2008). Seismic imaging of southwest Japan using P and PmP data: Implications for arc magmatism and seismotectonics. *Gondwana Research*, *14*(3), 535–542. https://doi.org/10.1016/j.gr.2008.04.004
Tape, C., Liu, Q., Maggi, A., & Tromp, J. (2009). Adjoint tomography of the southern California crust. *Science*, *325*, 988–992. https://doi.org/10.1126/science.1175298
Tape, C., Plesch, A., Shaw, J. H., & Gilbert, H. (2012). Estimating a continuous Moho surface for the California unified velocity model. *Seismological Research Letters*, *83*(4), 728–735. https://doi.org/10.1785/0220110118
Tong, P., Yang, D., Huang, & Xueyuan (2019). Multiple-grid model parametrization for seismic tomography with application to the San Jacinto fault zone. *Geophysical Journal International*, *218*(1), 200–223. https://doi.org/10.1093/gji/ggz151
Trnkoczy, A. (1999). Topic Understanding and parameter setting of STA/LTA Trigger Algorithm. *New manual of seismological observatory practice*, *2*.
Wang, H., Zhao, D., Huang, Z., Xu, M., Wang, L., Nishizono, Y., & Inakura, H. (2018). Crustal tomography of the 2016 Kumamoto earthquake area in West Japan using P and PmP data. *Geophysical Journal International*, *214*(2), 1151–1163. https://doi.org/10.1093/gji/ggy177
Wang, X., Chen, Q. F., Li, J., & Wei, S. (2016). Seismic sensor misorientation measurement Using P-wave Particle motion: An application to the NECsaids Array. *Seismological Research Letters*, *87*(4), 901–911. https://doi.org/10.1785/0220160005
Wessel, P., & Smith, W. H. (1998). New, improved version of generic mapping tools released. *Eos, Transactions American Geophysical Union*, *79*(47), 579. https://doi.org/10.1029/98eo00426
Wright, T. J., Elliott, J. R., Wang, H., & Ryder, I. (2013). Earthquake cycle deformation and the Moho: Implications for the rheology of continental lithosphere. *Tectonophysics*, *609*, 504–523. https://doi.org/10.1016/j.tecto.2013.07.029
Xia, S., Zhao, D., Qiu, X., Nakajima, J., Matsuzawa, T., & Hasegawa, A. (2007). Mapping the crustal structure under active volcanoes in central Tohoku, Japan using P and PmP data. *Geophysical Research Letters*, *34*(10), L10309. https://doi.org/10.1029/2007gl030026

Xu, M., Huang, Z., Wang, L., Xu, M., Zhang, Y., Mi, N., & al, e. (2020). Sharp lateral Moho variations across the SE Tibetan margin and their implications for plateau growth. *Journal of Geophysical Research: Solid Earth*, *125*, e2019JB018117. https://doi.org/10.1029/2019jb018117

Yan, Z., & Clayton, R. W. (2007). Regional mapping of the crustal structure in southern California from receiver functions. *Journal of Geophysical Research*, *112*(B5), B05311. https://doi.org/10.1029/2006jb004622

Youssof, M., Thybo, H., Artemieva, I. M., & Levander, A. (2013). Moho depth and crustal composition in Southern Africa. *Tectonophysics*, *609*, 267–287. https://doi.org/10.1016/j.tecto.2013.09.001

Zhao, D. (2019). Importance of later phases in seismic tomography. *Physics of the Earth and Planetary Interiors*, *296*, 106314. https://doi.org/10.1016/j.pepi.2019.106314

Zhu, L. (2000). Crustal structure across the San Andreas Fault, southern California from teleseismic converted waves. *Earth and Planetary Science Letters*, *179*(1), 183–190. https://doi.org/10.1016/s0012-821x(00)00101-1

Zhu, L. (2002). Deformation in the lower crust and downward extent of the San Andreas Fault as revealed by teleseismic waveforms. *Earth Planets and Space*, *54*(11), 1005–1010. https://doi.org/10.1186/bf03353293

Zhu, L., & Kanamori, H. (2000). Moho depth variation in southern California from teleseismic receiver functions. *Journal of Geophysical Research*, *105*(B2), 2969–2980. https://doi.org/10.1029/1999jb900322

Zhu, L., & Rivera, L. A. (2002). A note on the dynamic and static displacements from a point source in multilayered media. *Geophysical Journal International*, *148*(3), 619–627. https://doi.org/10.1046/j.1365-246x.2002.01610.x